Neoadjuvant Therapy Induced Upregulation of Complement Expression within Tumor Microenvironment is Associated with Immunomodulation and Survival Advantage in Pancreatic Ductal Adenocarcinoma: Insights from Spatially Transcriptomics

Running Title

Neoadjuvant Therapy Differentially Remodels Carcinoma and Tumor Microenvironment in Pancreatic Ductal Adenocarcinoma: Insights from Spatially Transcriptomics

Xiaofei Zhang[1#]*, Ruoxin Lan[2#], Yongjun Liu[3], Venu G Pillarisetty[4], Danting Li[2], Chaohui L Zhao[1], Suparna A. Sarkar[5], Weiguo Liu[1], Iman Hanna[1], Mala Gupta[1], Cristina Hajdu[5], Jonathan Melamed[1], Jessica Widmer[6], John Allendorf[7], Yao-Zhong Liu[2]*

1. Department of Pathology and Laboratory Medicine, 6. Department of Gastroenterology, 7. Department of Surgery, New York University Grossman Long Island School of Medicine, Long Island, NY

2. Department of Biostatistics and Data Science, Tulane University School of Public Health and Tropical Medicine, New Orleans, LA

3. Department of Laboratory Medicine and Pathology, 4. Department of Surgery, University of Washington School of Medicine, Seattle, WA

5. Department of Pathology and Laboratory Medicine, New York University Grossman School of Medicine, New York, NY

#: Co-first authors

*: Co-corresponding authors

Abstract

Neoadjuvant therapy (NAT) is increasingly used in the treatment of pancreatic ductal adenocarcinoma (PDAC). However, it is insufficiently understood how it differentially impacts carcinoma and tumor microenvironment (TME). We separately compared gene expression profiles in carcinoma and TME between NAT-treated versus NAT-naive patients using spatial transcriptomics. We found that NAT enhances apoptosis and reduces proliferation of carcinoma cells and profoundly remodels TME. Notably, several key complement genes (C3, C1S, C1R, C4B and C7) were coordinately upregulated in TME, making complement pathway the most significantly altered pathway by NAT. Furthermore, patients with a more pronounced increase of TME complement gene expression after receiving NAT demonstrated improved overall survival, more immunomodulatory and neurotropic cancer-associated fibroblasts (CAFs), increased $CD4^+$ T cells and mast cells, and reduced immune exhaustion. These findings suggest that NAT may alleviate immunosuppression by upregulating complement signaling in TME, which could be a novel biomarker for prognostication and stratification of NAT-treated PDAC patients.

Keywords: Pancreatic ductal adenocarcinoma (PDAC), Neoadjuvant therapy (NAT), Tumor microenvironment (TME), Complement, Immune exhaustion, Spatial Transcriptomics

INTRODUCTION

Pancreatic ductal adenocarcinoma (PDAC) is a highly aggressive cancer with a five-year survival rate of only 11% [1]. It is projected to become the second leading cause of cancer-related deaths in the United States by 2030 [2]. Only 15-20% of patients are eligible for surgery, as most patients present with locally advanced unresectable disease or distant metastases[3]. Furthermore, since most patients who undergo surgical resection ultimately succumb to their disease, systemic chemotherapy is a necessary therapeutic component for most patients [4].

PDAC presents a significant therapeutic challenge due to its resistance to various treatment modalities including immune checkpoint inhibitor therapy [5]. It exhibits extensive genetic diversity, leading to the development of subpopulations with diverse molecular alterations and resistance mechanisms [6]. The tumor microenvironment (TME) in PDAC is highly immunosuppressive, characterized by the presence of immunosuppressive cells, cytokines, and chemokines that impede effective anti-tumor immune responses despite the presence of large numbers of effector T cells [7 8]. These factors collectively contribute to the high resistance observed in PDAC, highlighting the need for innovative combinational strategies to improve treatment outcomes.

Neoadjuvant therapy (NAT) has emerged as the preferred approach for managing resectable and borderline resectable PDAC over adjuvant therapy at many institutions for several reasons. Firstly, NAT offers better tolerability for patients by administering chemotherapy and/or radiation prior to surgery, taking advantage of patients' relatively better health status and minimizing treatment-related complications [9,10]. Secondly, NAT effectively increases tumor resectability and R0 resection rate by downstaging locally advanced disease and facilitating complete tumor removal [11,12]. Moreover, NAT targets early metastasis, potentially improving treatment outcomes [11,12]. It also provides an opportunity to observe an individual patient’s response to therapy for selecting suitable candidates for surgery [11,12]. Recently, some studies suggested that NAT may be associated with improved overall survival rates compared to adjuvant therapy [9,10]. Furthermore, some recent studies suggested that NAT may have the

potential to prime the stroma and enhance the response to immunotherapy in various cancers [13]. By modulating TME, NAT may render PDAC more susceptible to immunotherapeutic interventions [13].

Single-cell RNA sequencing (scRNA-seq) is a valuable tool for characterizing TME as it provides insights into cellular heterogeneity and molecular subtypes [14,15]. Several scRNA-seq studies have explored the PDAC TME, offering valuable insights into this complex ecosystem [16-20]. However, scRNA-seq techniques lack spatial context, and are susceptible to cell dissociation-associated artifacts. Spatial transcriptomic analysis complements and extends the scope of single-cell studies [21] by providing valuable insights into the spatial distribution of gene expression and a holistic characterization of the PDAC TME. To obtain a comprehensive view of the PDAC TME and its response to NAT, we performed a spatial transcriptomic comparative study on formalin-fixed paraffin-embedded (FFPE) specimens from PDAC patients who received NAT before surgery versus those who underwent upfront surgery without NAT.

RESULTS

Intra- and intertumoral heterogeneity of NAT response in PDAC carcinoma and TME

The clinicopathologic characteristics of the 36 patients in our study cohort are summarized in Figure 1A and Supplementary Table 1. This cohort includes 13 patients who had upfront surgery (the naïve group) and 23 age-, gender-, and stage-matched patients who had surgery after receiving neoadjuvant chemotherapy (the NAT group), which consisted of either FOLFIRINOX or gemcitabine treatment, with or without radiation. Only resected primary PDAC specimens were used in this study except for 4 patients in NAT group whose pre-NAT biopsies were included in the naïve group. A separate pairwise longitudinal comparison of the pre-NAT biopsy versus the post-NAT resection from the same patient was also done for these 4 patients (Supplementary Tables 2). To assess the relative extents of intra- vs. intertumoral heterogeneity, 2 to 5 ROIs (region of interest) were selected from each case, amounting to a total of 119 ROIs (Supplementary Figure 1). Using immunofluorescence staining, we

segmented each ROI into two AOIs (area of illumination): the carcinoma AOI (pan-CK+, SMA-) containing only malignant cells, and the TME AOI (pan-CK-, SMA+) which comprised of various types of stroma cells and immune cells (Figure 1B). RNA libraries were prepared from these 238 AOIs, of which 223 (93.7%) passed the quality control and were used for spatial transcriptomics analysis, which including 42 carcinoma AOIs and 43 TME AOIs from the naïve group, and 72 carcinoma AOIs and 66 TME AOIs from the NAT group.

First, we compared the gene expression profiles between carcinoma AOIs vs. TME AOIs. Carcinoma AOIs showed significantly higher expression of 302 and 321 genes than TME AOIs in the naïve group and the NAT group, respectively, with an overlap of 261 genes that included *KRT19, KRT7, KRT18, MUC1, CDH1, EPCAM, JUP, ITGA3, ITGB4, ERRB2, LAMB3, CAPN2, LGALS3, LCN2* etc. In contrast, TME AOIs showed significantly higher expression of 286 and 294 genes than carcinoma AOIs in the naïve group and the NAT group, respectively, with an overlap of 250 genes including *PDGFRB, COL6A3, FCGR2A/B, IL1R1, etc.* (Supplementary Figure 2, Supplement Data 1). Hierarchical clustering analysis successfully grouped these 223 AOIs into distinct carcinoma and TME clusters, with a limited number of datapoints appearing in between these two distinct clusters. Conversely, no discernible differentiation was observed between the naïve and NAT AOIs within both the carcinoma AOI cluster and TME AOI cluster (Figure 1C).

Subsequently, we used a dimension reduction technique to visualize the clustering pattern of these 223 AOIs in two major UMAP dimensions based on their transcriptomics profile. Similar to the results from the hierarchical clustering analysis, these 223 AOIs were largely separated into carcinoma cluster and the TME cluster, with only a limited number of AOIs from each category intermingling at the peripheries of these two clusters (Figure 1D). However, notable differentiation based on treatment status (i.e., naïve vs. NAT) was once again not evident, suggesting both carcinoma and TME responded to NAT heterogeneously at the transcriptomics level.

To further investigate the roles of intra/intertumoral heterogeneity in NAT response, we also made a UMAP plot of the four pairs of samples in which pre-NAT biopsies were compared with post-NAT resections from the same patient. In addition to the clear separation of carcinoma AOIs from TME AOIs, a separation was also noted between the naïve group (i.e., pre-NAT biopsy) and the NAT group (i.e., the post-NAT resection) in both carcinoma AOI cluster and TME AOI cluster (Figure 1E). In accordance with the anticipated relative magnitudes of intra- vs. intertumoral heterogeneity, the AOIs from the same patient tended to aggregate more closely together than those from different patients.

To compare the cellular composition within carcinoma AOIs and TME AOIs, we calculated the gene signature scores for different types of immune cells, fibroblasts and other stromal cells using our transcriptomics data. As compared to carcinoma AOIs, TME AOIs contained significantly more fibroblasts and immune cells across the board (Supplementary Figure 3).

Effects of NAT on PDAC carcinoma

We studied the effect of NAT on PDAC carcinoma cells by comparing the gene expression profiles in the carcinoma AOIs of the naïve group versus the NAT group. After controlling for age, gender and other clinicopathological factors, we identified 44 NAT-induced differentially expressed genes (DEGs) in carcinoma AOIs, including 22 upregulated and 22 downregulated (Figure 2A, Supplementary Data 2). The topmost significantly upregulated genes include *DDB2* (p = 7.70e-4), *FBP1* (p= 0.0016) and *PRKACB* (p = 0.0028). The topmost significantly downregulated genes include *IL32* (p =0.0039), *ACTB* (p = 0.0041) and *TPM1* (p = 0.0059). DAVID enrichment analysis of these DEGs indicated that the upregulated genes in the carcinoma cells of NAT-treated PDAC were significantly enriched with functional terms related with apoptosis (KW-0053~Apoptosis, FDR = 0.013) and Ser/Thr-type protein kinases (SM00133:S_TK_X, FDR = 0.024), suggesting upregulation of these functional terms by NAT (Figure 2B). On the other hand, the downregulated genes in carcinoma cells of NAT-

treated PDAC were significantly enriched with functional terms related to chromatin (GO:0000785~chromatin, FDR = 0.0059), nucleoplasm (GO:0005654~nucleoplasm, FDR = 0.023), GO:0032991~macromolecular complex (FDR = 0.023), and KW-0488~Methylation (FDR = 0.024) (Figure 2B), suggesting downregulation of these functional terms by NAT. These results are consistent with the expected cytoreductive effect of neoadjuvant chemotherapy on carcinoma cells.

Next, we delved deeper into the impact of NAT on carcinoma cells utilizing the recently defined gene signatures for seven malignant cell programs representing the lineages of carcinoma cells and seven malignant cell states[19]. Signature scores for each of these malignant programs and cell states were calculated for all carcinoma AOIs based on the geometric mean expression levels of their respective signature genes set. Their association with NAT was assessed after controlling for age, gender, cancer grade and stage. We found that there was a significant increase of acinar-like program (p = 0.011, Figure 2C) and a significant decrease of cyclining_G2/M state (p = 0.001), along with a marginally significant decrease of TNF-NFkB signaling (p = 0.057) in the NAT group. These findings were also supported by our morphologic analysis, which showed increased apoptosis along with decreased proliferation and mitosis of the carcinoma cells in the NAT group compared to the naïve group (Figure 2D).

Effects of NAT on the PDAC TME

Next, we examined the effect of NAT on PDAC TME by comparing the gene expression profiles of the TME AOIs between the naïve group versus the NAT group. After controlling for age, gender, carcinoma grade and stage; we identified 52 NAT-induced DEGs in the TME AOIs, including 28 upregulated and 24 downregulated (Figure 3A, Supplementary Data 3). The top significantly upregulated genes include *CDKN1A* (p=3.82e-4), *MDM2* (p=8.04e-4), *FAS* (p = 2.72e-3) and *IL6ST* (p = 0.0055). The top significantly downregulated genes include *HDAC2* (p = 2.84e-5), *TPM1*(p=7.21e-4), *ACTB* (p = 2.28e-3) and *PKM* (p = 0.0033). Remarkably, there were five complement genes (*C1S, C1R, C3, C4B* and

C7) among the most significantly upregulated genes, suggesting that NAT induced a coordinated upregulation of complement pathway genes in PDAC TME.

DAVID enrichment analysis of these significantly upregulated DEGs showed that NAT upregulated more functional terms in TME than in carcinoma of PDAC (Figure 3B). Among those, there were three highly enriched terms related to complement pathway, including KW-0180~Complement pathway (FDR = 1.04e-5); GO:0006958~Complement activation, classical pathway (FDR = 1.06e-2); and has04610~Complement and coagulation cascades (FDR = 1.28e-3). Additionally, there were functional terms related to immunity, including KW-0399 Innate immunity (FDR = 9.61e-3); KW-0391 Immunity (FDR = 5.04e-2); and multiple pathways related to cancer, e.g., hsa04115 p53 signaling pathway (FDR = 1.73e-4) (Figure. 3B). To illustrate the gene components for these enrichment terms, chord maps for the most significantly enriched GO, KEGG and UP_KW functional terms were made. The 5 complement genes (C1S, C1R, C3, C4B and C7) contribute to not only complement-related pathways, but also other key functional terms related to immunity and innate immunity (Figure 3 C). These findings imply that NAT-induced upregulation of complement expression within TME may contribute to the overall immunomodulation in PDAC.

Subsequently, we studied the effect of NAT on the cancer-associated fibroblasts (CAFs) within PDAC TME using the expanded CAF classification system recently defined by Hwang et al. in 2022[19], in which CAFs are categorized into 4 subtypes, including adhesive, immunomodulatory, myofibroblastic, and neurotrophic. By assessing the geometric mean expression levels of signature genes for each subtype, we computed signature scores for all four subtypes of CAFs within each TME AOI and analyzed the association with NAT treatment while controlling for age, gender, carcinoma grade and stage. We found that immunomodulatory (p=0.023) and neurotropic CAFs (p=0.002) were significantly increased in the TME of the NAT group as compared to the naïve group (Figure 4A). Additionally, there was a strong linear dependence (p=1.80e-5) of complement C3 expression level on the signature score of immunomodulatory CAFs in TME (Figure 4B), suggesting that the increase of immunomodulatory CAFs

may be one of the major contributing factors for NAT-induced upregulation of complement within TME (Figure 4B).

To investigate NAT's effect on the tumor immune microenvironment (TIME), signature scores for all major immune cell types were calculated for each TME AOI and tested for association with NAT treatment while controlling for age, gender, carcinoma grade and stage. There was no statistically significant change of signature scores for most types of immune cells in the TME of the NAT group compared to the naïve group, except for mast cells which were increased with a marginal statistical significance (p=0.09) (Figure 4C). Histologic analysis showed that there were increased number of CD117+ cells in the TME of NAT-treated PDAC as compared to naïve PDAC (Figure 4D).

NAT-induced upregulation of TME complement expression is associated with improved survival and immunomodulation

To explore the clinical and prognostic implications of NAT-induced upregulation of TME complement, we stratified NAT group in our cohort into high complement subgroup (9 out of 23 NAT-treated patients) and low complement subgroup (14 out of 23 NAT-treated patients) based on a clustering analysis of the mean expression levels of the 5 NAT-upregulated complement genes (C3, C4, C7, C1S and C1R) within TME (Figure 5A). Kaplan-Meier analysis revealed that patients in the high complement subgroup exhibited a significantly better overall survival compared to patients in low complement subgroup (p=0.023) (Figure. 5B). Moreover, when contrasted with the naïve group, while patients from the low complement subgroup displayed no significantly different overall survival rates, patients from the high complement subgroup exhibited a marginally improved survival trend ($p<0.1$) (Figure. 5B). Importantly, multivariate Cox proportional hazard ratio analysis confirmed that that a high TME complement level emerged as an independent favorable prognostic factor (hazard ratio = 0.21; 95% Confidence Interval (CI): 0.06 to 0.81) for NAT-treated patient (Figure. 5C). Conversely, a positive

surgical resection margin (R1) serves as an independent adverse prognostic factor (HR=5.45, 95% CI=1.28-23.27) (Figure. 5C).

To further explore the survival advantages associated high TME complement level, we also investigated the correlation between TME complement C3 level and overall survival in those 4 patients for whom we had both pre-NAT biopsy and post-NAT resection for paired analysis. Among these 4 patients, two exhibited significantly increased TME C3 level following NAT and demonstrated improved overall survival as compared to the rest two patients who did not show increase of TME C3 complement level following NAT (Supplementary Figure. 5). These results suggest that patients with a significant upregulation of TME complement level in response to NAT may experience improved overall survival.

To understand the mechanism underlying the association between the NAT-induced upregulation of TME complement and the survival advantage, we compared signature scores of immune cells and CAFs in the TME of the high TME complement subgroup versus the low TME complement subgroup. Our analysis revealed that the high TME complement subgroup showed significantly higher signature scores for mast cell ($p = 0.037$) and $CD4^+$ T cells ($p = 0.039$) compared to the low TME complement subgroup (Figure. 6A). As expected, the signature scores for immunomodulatory CAF ($p = 3.46e-4$, Figure. 6B) and neurotrophic CAF ($p = 6.88e-3$) were also significantly increased. Notably, the high TME complement subgroup also showed a significant reduction of immune exhaustion signature ($p = 0.038$) without a significant change in immune cell cytotoxicity score (Figure. 6B). These results suggest that NAT-induced upregulation of TME complement may mitigate immune exhaustion and reduce immunosuppression in PDAC (Figure 6C).

Discussion

Our results revealed that NAT differentially remodels carcinoma and TME of PDAC through different targets and mechanisms. By doing a comprehensively analysis of the gene expression profiles of

>1800 selected genes related to cancer biology, TME and immune responses, we discovered that NAT induced 44 DEGs in the carcinoma cells and 52 DEGs in the TME when comparing the spatial transcriptomics profiles of NAT-treated PDAC versus NAT-naïve PDAC. Gene set enrichment analysis revealed 9 significantly up- or downregulated gene sets and functional terms in carcinoma cells, in contrast to 61 in the TME of treated PDAC. These results indicate that NAT may have a more extensive and profound effect on the TME than on the carcinoma cells per se. In the carcinoma cells of NAT-treated PDAC, most DEGs are linked to the regulation of apoptosis, cell cycle regulation and DNA repair. Among them, the most significantly upregulated DEG was *DDB2* (p=0.00077), which encodes DNA damage-binding protein 2, a nuclear protein crucial for DNA repair and genomic stability. Additionally, DDB2 has been shown to suppress epithelial-to-mesenchymal transition (EMT) and enhance sensitivity to chemotherapy in PDAC [22]. In contrast, in the TME of NAT-treated PDAC, most DEGs are linked to complement signaling and regulation of innate and adaptive immune function. Among them, the most significant downregulated DEG was *HDAC2*, which encodes Histone deacetylase 2, a transcription factor capable of inducing inflammatory gene expression in CAFs and supporting carcinoma growth in PDAC. Recent studies have demonstrated the role of HDAC2 in facilitating pancreatic cancer metastasis [23].

Notably, we observed a coordinated upregulation of five key complement genes (C3, C4B, C7, C1R, C1S) in the TME of NAT-treated PDAC as compared to those not treated by NAT. Due to the collective upregulation of these five complement genes, the complement pathway emerged as the most significantly enriched pathway (FDR=1.04×10^{-5}) among the NAT upregulated gene sets. It is worth noting that this NAT-induced upregulation of complement expression was spatially confined to the TME. Traditionally, complement proteins were primarily considered to be produced in the liver and circulating in the bloodstream to aid the immune function by opsonization [24]. However, our results suggest that the complements may also be produced locally within TME and play an important role in regulating immune response. Although our method could not determine the specific cell types within TME responsible for producing complement proteins, our data did reveal that NAT significantly increased the expression of

signature genes associated with immunomodulatory type CAFs (Figure 4A). This increase was particularly prominent in patients with high TME complement expression following NAT treatment (Figure 5D). Additionally, we found a strong dependence of the TME C3 complement level on the signature score of immunomodulatory CAFs, suggesting that this specific subtype of CAFs is likely one of the main factors contributing to the local production of complement proteins within PDAC TME.

Our findings align with several recent single-cell or single-nucleus RNA-seq studies. In 2021, Chen et al. identified a distinctive subtype of CAF termed “complement-secreting CAFs” (cs-CAFs) that are characterized by their enrichment with complement system genes. They found that cs-CAFs were predominantly located near malignant glands, and mainly existed in early-stage PDAC and diminished in late-stage PDAC [25]. More recently, Croft et al. demonstrated that some CAFs located farther from malignant glands can also produce complement proteins, and their increase was associated with improved patient survival [26]. In 2022, Hwang et al. expanded the CAF classification to include four subtypes: adhesive, immunomodulatory, myofibroblast, and neurotrophic. They found that only immunomodulatory CAFs were enriched with complement genes [19]. In a separate study, Werba et al. also observed complement gene enrichment in inflammatory CAFs [20]. However, none of these single-cell or single-nucleus RNA-seq studies specifically investigated the impact of NAT on complement gene expression within TME. Our research, for the first time, demonstrates a link between NAT-induced upregulation of TME complement and increased expression of gene signatures of immunomodulatory CAFs. Further studies, especially those using single-cell spatial transcriptomics, are warranted to characterize how NAT influences the distribution and adaptability of immunomodulatory CAFs. In fact, a recent study by Shiau et al. using single cell spatial transcriptomics revealed that NAT induced significant changes in interaction strength between malignant cells and inflammatory CAFs, driven by enriched IL-6ST signaling [27], which is also one of the most significantly upregulated genes in the TME of NAT-treated PDAC discovered in our study (Figure 3A and 3C).

Another interesting finding of our study is that NAT-induced upregulation of complement expression in the TME is associated with modulation of the TIME, manifested as increased immune cell infiltration (including mast cells etc.) and decreased expression of immune exhaustion markers (Figure 5D). Importantly, the NAT-treated patients with higher TME complement demonstrated improved overall survival (Figure 5B). The detailed cellular and molecular mechanisms underlying these observations are yet to be further clarified. It is known that some cleaved complement proteins (such as C3a, C5a, etc.) are potent chemoattractants and can recruit immune cells into TIME. Recent evidence has also indicated that a tonic level of complements in TME is required for maintaining immune cell homeostasis and function via the non-canonical intracellular complement (i.e., composure) signaling [28]. Our data suggests that TME complement may serve as a regulatory hub in the local tumor microenvironment for both innate and adaptive immune functions via both canonical and non-canonical signaling mechanisms. Further studies are warranted to elucidate the specific details of this novel mechanism.

Our study is the first spatial transcriptomics study specifically designed to compare the differential remodeling effect of NAT on carcinoma cells and the TME using FFPE tissue of a relatively large cohort of resected primary PDAC. The main limitation of our study is that the spatial transcriptomics method used is not at single-cell level. On the other hand, since there is no cell isolation and processing needed as in single-cell or single-nucleus RNA-seq, the method we used in this study may suffer from less technical variability and batch effect, and not impacted by the artifactual transcriptomics changes secondary to the procedure-induced cell stress. This is especially important for PDAC in which all cellular components are buried in excessive dense extracellular matrix which makes cell isolation particularly challenging. In addition, because mRNAs from each AOI were pooled together, the higher mRNA concentration in each sample provides deeper reads and fewer dropouts, yielding a better signal-to-noise ratio and more robust detection for weakly expressed genes. Recently, the single-cell RNA-seq study by Werba et al observed generally decreased cell-cell interaction and high volume of putative interactions between CAFs and tumor-associated macrophages (TAMs) in the TME of NAT-treated

PDAC[20]. No difference was noted in CAF subpopulation distributions between NAT-treated vs. naive groups [20]. Hwang et al. discovered that NAT could increase the adhesive CAFs and decrease the myofibroblast CAFs. They also found that the number of immunomodulatory CAFs was higher in patients treated with regular NAT than those with NAT plus losartan [19]. In the most recent study using single-cell spatial transcriptomics, Shiau et al showed that a marked increased ligand-receptor interaction between CAFs and malignant cells in NAT-treated PDAC[27]. Therefore, our data have not only confirmed previous single-cell RNA-seq studies but also provided additional valuable insights thanks to the preserved spatial context.

In conclusion, by using spatially resolved transcriptomics, we demonstrated that NAT affects the carcinoma and the TME of PDACs through different mechanisms. NAT can significantly upregulate complement gene expression within TME, which is associated with reduced immune exhaustion and improved survival. These results suggest that NAT may have the potential to mitigate immune cell exhaustion and enhance immune surveillance in some PDAC patients. Those patients who did not respond to NAT with a significant upregulation of TME complement may have more immune exhaustion and thus benefit from combinational immune checkpoint blockade therapy. Therefore, assessment of TME complement levels may provide more accurate prognostic guidance for NAT-treated patients, which may help to stratify them for more tailored downstream interventions. Further analyses, especially spatial transcriptomics at the single cell resolution, are warranted to elucidate the detailed cellular and molecular mechanisms of complement-mediated immunomodulation and its potential therapeutic implications.

Methods

Patient cohort and data collection

All patient selection and data collection procedures were reviewed and approved by the University of Wisconsin – Madison Institutional Review Board. The study's inclusion criteria were adult patients with non-metastatic PDACs who had surgery at the University of Wisconsin–Madison Hospital between 2015 to 2020. Patients with incomplete clinicopathologic information or incomplete archived slides or tissue blocks were excluded. A total of 36 patients met the inclusion criteria and were used in our cohort for this study, including 13 patients who had upfront surgery without any forms of NAT and 23 patients who had NAT (either chemotherapy alone or in combination with radiation) before surgery. In call cases, patients had at least 38 months of clinical follow-up. The pertinent clinicopathological information, including age, gender, carcinoma size, regime of NAT, type of surgery, pathological grade and stage, and treatment response, were collected by retrospective reviewing of electronic medical records. Among the 23 patients in the NAT group, 16 patients received multiple cycles FOLFORINOX, and 7 patients received gemcitabine and Abraxane. Eight patients received concurrent radiation therapy. For all patients, only resection specimens were used, except for 4 patients, from whom the pre-NAT biopsies were also included for a pared longitudinal comparison with their corresponding post-NAT resection samples. After reviewing all slides, one section with the most representative histology section was selected from each case for spatial transcriptomics study and morphology analysis.

Histology and immunohistochemistry

Serial sections (4 μm in thickness) were cut from the selected formalin-fixed, paraffin-embedded (FFPE) tissue block for the consecutive staining of H&E, immunofluorescence staining for DSP (Digital Spatial Profiler) experiment, and immunohistochemistry staining. For immunohistochemistry, sections were stained using the Roche Ventana Medical System's Discovery Ultra Automated Platform (Roche Diagnostics). All reagents were Roche-Ventana proprietary reagents except for the Harris Modified

hematoxylin (ThermoFisher). After deparaffinization, heat-induced epitope retrieval was done with CC1 buffer (Ventana, #950-224) for approximately 32 minutes at 95ºC. Then, slides were incubated with the primary antibodies. After reaction with HPR and DAB, all slides were counterstained with hematoxylin, and digitized by Aperio Digital Pathology Scanner (Leica) at 40x magnification. Digital pathology analysis was carried out using QuPath (v0.4.3) and HALO (Ver 3.6, IndicaLab).

Sample preparation for NanoString GeoMx DSP

For DSP experiment, sections were baked at 60ºC for 1.5 hours and deparaffinized in CitriSolv. After rehydration, sections were incubated in 100 °C 1x Tris-EDTA/pH 9 buffer for 15 minutes for antigen retrieval. After digestion and post-fixation, all sections were hybridized to UV-photocleavable barcode-conjugated RNA in situ hybridization probe set (Nanostring CTA, 1812 gene targets) overnight at 37 °C. Then, all slides were washed to remove off-target probes. Next, slides were used for immunofluorescence staining with morphology markers set, which contains 1:10 SYTO13 (Thermo Fisher Scientific, cat. no. 57575), 1:20 anti-panCK-Alexa Fluor 532 (clone AE-1/AE-3; Novus Biologicals, cat. no. NBP2-33200AF532), and 1:100 anti-αSMA-Alexa Fluor 647 (clone 1A4; Novus Biologicals, cat. no. IC1420R) in blocking buffer (NanoString). The immunofluorescence images were scanned for the segmentation of the carcinoma AOI (area of illumination, panCK+, SMA-) and the TME AOI (panCK-, SMA+). For each slide, 2–5 ROIs (Regions of Interest) with the most representative morphology were selected. Photocleavage of spatially indexed barcode and sample collection were done on GeoMx DSP equipment (NanoString). Samples obtained from each AOI were collected in a 96-well plate. RNA Libraries were prepared according to the manufacturer's instruction. Then, Next Generation Sequencing (NGS) read-out was done using an Illumina NextSeq 550AR sequencer. The data was exported as digital count conversion (DCC) files which were used for analysis using R and Bioconductor packages.

Data pre-processing and normalization

We followed a published online R and Bioconductor GeoMx-NGS workflow (NanoString Technologies, Inc) for QC (quality control), pre-processing and normalization of raw GeoMx DSP count files and metadata. The website of the workflow is at https://bioconductor.org/packages/devel/workflows/vignettes/GeoMxWorkflows/inst/doc/GeomxTools_RNA-NGS_Analysis.html .

In brief, the workflow included data loading (of DCC, PKC and annotation files), and illustration of study design using Sankey diagram (Supplemental Figure 1). The loaded data then underwent QC and pre-processing steps, including segment QC for every AOI segment (e.g., removing segments with >1,000 raw reads and those with less than 80% rate for % aligned, % trimmed or % stitched), probe QC to remove low-performing probes, creation of gene-level count data by combining counts across multiple probes of a gene via geometric mean, and determination of limit of quantification (LOQ) of each segment based on the distribution of negative control probes. Based on the calculated LOQ, the number of detected genes was decided for each segment and segment-wise gene detection rate was inferred, and those segments with less than 1% of gene detection rate were removed. Similarly, the detection rate for each gene across the study was determined and those genes detected in only 5% or less of all segments were removed.

Based on the filtered gene expression matrix, the GeoMx data were normalized using Q3 (3rd quartile) normalization. The Q3 normalized data were then used for downstream data analyses, as detailed below.

Unsupervised analysis

The UMAP method was used to visualize the segment-level data in two major dimensions (UMAP1 and UMAP2) by using the UMAP R package. Unsupervised hierarchical clustering of all genes was performed using pheatmap package by first conducting log2 transforming the data, followed by selecting highly variable genes (i.e., those of top 20 percentile of coefficient of variation of gene expression) to be included in the cluster heatmap. Similarly, unsupervised hierarchical clustering of 5

complement genes was performed with the pheatmap package using subject-wise average of gene expression value in the TME.

Differential expression analysis

Linear modeling analysis implemented in R was conducted to detect the effect of NAT on gene expression in either the carcinoma or the TME components. Specifically, the log2 transformed subject-wise average of gene expression of carcinoma or TME was modeled as the dependent variable, with independent variables including treatment status (i.e., NAT vs. naïve), age, gender, pathology grade and stage of the tumor. The estimate as well as the p value for the regression coefficient for treatment status (NAT-treated vs. naïve) was used to represent the effect of differential expression induced by NAT. To illustrate the differential expression, volcano plots were made with EnhancedVolcano package (version 1.13.2).

Signature scores for immune and fibroblast cell types

Signature scores for immune cell types of each AOI were imputed from the gene expression matrix with SpatialDecon package (version 1.4.3). Scores for other signature scores, including Malignant State Programs (i.e., cycling (S), cycling (G2/M), MYC signaling, adhesive, ribosomal, interferon signaling and TNF-NFkB signaling), Malignant Lineage Program (i.e., acinar-like, classical-like, basaloid, squamoid, mesenchymal, neuroendocrine-like, neural-like progenitor) and Fibroblast Programs (i.e., adhesive, immunomodulatory, myofibroblastic and neurotropic), were inferred based on geometric average of signature genes as described by Hwang et al. in 2022[19]. The signature score for Immune Exhaustion was inferred from the signature genes as provided in Werba G et al., in 2023 [20]. The same linear modeling analysis was used to test the effect of NAT on the above inferred signature scores.

Gene set enrichment analysis

The differentially expressed genes with p value < 0.05 were submitted to DAVID enrichment analysis [29,30]portal (https://david.ncifcrf.gov/home.jsp) for gene set enrichment analysis. To infer up- or downregulated gene sets, the up- or downregulated genes were submitted for analysis separately. To

visualize the enriched gene sets, dot plots were made with ggplot2 R package (v3.4.2) and chord maps were plotted with GOplot package (v1.0.2).

Survival analysis

R packages, survival (v3.5.5) and survminer (v0.4.9), were used to make Kaplan Meier (KM) survival curve and compare and test significance for the difference of survival between groups of patients. Specifically, the Cox Proportional Hazards Model was used to test the significance of survival differences in groups of patients while controlling for age, gender, tumor size and cancer grading.

Digital pathology analysis

All H&E slides and immunohistochemistry slides were digitized by whole slide scanning at 40X magnification using Leica Aperio AT2 DX from Leica. All digital pathology analysis was done using QuPath (version 0.4.3). Numbers of immunostaining positive cells were quantified by object classification function.

Data availability

The spatial transcriptomics data used here along with the metadata were submitted to NCBI GEO (Gene Expression Omnibus) with an accession number of GSE240078.

Acknowledgement

The authors thank the University of Wisconsin Translational Research Initiatives in Pathology laboratory (TRIP), supported by the UW Department of Pathology and Laboratory Medicine, UWCCC (P30 CA014520) and the Office of The Director- NIH (S10 OD023526) for use of its facilities and services. The authors also thank Nancy Liu for the artistic illustration in Figure 6C summarizing the main findings of this study.

Author contributions

X.Z., Y.Z.L., and Y.L. developed the study concept and the study design. X.Z., Y.Z.L., Y.L., and R.L. wrote the manuscript, which was then edited by all co-authors. X.Z. acquired slides and tissue blocks, collected patient information, and helped with the GeoMx experiment. X.Z. and D.L. analyzed the H&E and multiplex IHC. R.L., Y.Z.L, and X.Z. analyzed spatial transcriptomics data and conducted statistical analysis of clinicopathological information. V.G.P. provided feedback on the study design and the manuscript. C.L.Z., S.A.S., W.L., I.H., M.G., C.H., J.M., J.W., and J.A. provided feedback and edited the manuscript. All co-authors approved the final version of the manuscript before submission.

Competing interests

The authors declare no competing interests.

Figure Legends

Figure. 1 Intratumorally and intertumoral heterogeneity in NAT response in PDAC carcinoma and TME revealed by spatial transcriptomics. A. Clinical and pathologic characteristics of the 36 patients in our study cohort. For patients 14, 15, 16 and 17, pre-NAT biopsies were included in the naïve group, and the post-NAT resection specimens were included in the NAT group. For all other patients, only resected primary PDAC specimens were used. **B.** Immunofluorescence segmentation of each ROI into carcinoma AOI and TME AOI (pan-CK in green, α-SMA in yellow, DAPI in blue). RNA libraries were prepared separately from each of these two AOIs for every ROI. **C.** Heatmap of gene expression profiles in all 223 carcinoma and TME AOIs. Distinct separation between carcinoma AOIs and TME AOIs is evident in the unsupervised clustering analysis, with only a limited overlap. There is no discernible separation between the naïve group and the NAT group in either the carcinoma AOI cluster or the TME AOI cluster. **D.** UMAP plot demonstrating the near-complete separation of carcinoma AOIs (below the dashed line) and TME AOIs (above the dashed line). 95.1% (137/144) of the TME AOIs cluster above the dashed line, and 94.5% (103/109) of the carcinoma AOIs cluster below the dashed line. Approximately 5% of the AOIs overlap at the peripheries of these two clusters. There is no noticeable separation between the NAT group and the naïve group within either cluster. **E.** UMAP plot of the four pairs of pre-NAT biopsy (as naïve) and post-NAT resection (as NAT-treated) in patients 14, 15, 16, 17 (Δ=naïve carcinoma; ▲=NAT-treated carcinoma. ○=naïve TME; ●=NAT-treated TME. Datapoints for AOIs from the patient are shown in same color). For both carcinoma AOIs and TME AOIs, datapoints from NAT group are separated from those from the naïve group. The dashed lines connect each datapoint to its nearest neighbor. Most of the datapoints are closest to datapoint from the same subject, suggesting datapoints from the same patient tend to aggregate together.

Figure. 2 Effects of NAT on PDAC carcinoma. A. Volcano-plot showing up- and down- regulated genes in carcinoma cells induced by NAT. **B.** Chord map illustrating the relationship between the DEGs

and the enriched pathways. **C.** Impact of NAT on malignant cell lineage programs (left) and malignant cell states (right). NAT treatment significantly upregulated the acinar program and downregulated the cycling_G2/M state. TNF-NFκB signaling is also decreased with marginal statistical significance (* $p<0.05$; *** $p<0.001$, # $p<0.1$). **D.** Histologic evaluation confirming that the NAT-treated carcinoma cells show significantly increased apoptosis (solid arrowhead), decreased mitosis (open arrowhead), greater nuclear pleomorphism, and cytoplasmic vacuolization, in line with the transcriptomics findings.

Figure. 3 Effects of NAT on PDAC TME. A. Volcano plot showing the significantly up- and downregulated DEGs in TME induced by NAT. **B.** Dot Plots showing the most up- and downregulated pathways in TME induced by NAT. Three complement related pathways were significantly upregulated. **C.** Chord maps illustrating the interaction between the DEGs and the enriched pathways. The five NAT-upregulated complement genes are broadly associated with regulation of immune related pathways.

Figure 4. Effects of NAT on CAFs and immune cells in PDAC TME. A. NAT significantly increases immunomodulatory CAF and neurotrophic CAF in PDAC TME. There are no significant differences observed in adhesive CAF and myofibroblastic CAF between the NAT group and the naïve groups. (Tukey Box and Whisker plot, blue represents the naïve group, red represents the NAT-treated group.) **B.** Linear regression line showing a strong dependence of TME complement C3 expression level on the immunomodulatory CAF signature scores ($R=0.65$, $p=1.8e-05$). **C.** NAT-induced alterations in the cellular landscape in PDAC tumor immune microenvironment (TIME). Following NAT treatment, there is a marginal increase in mast cells. There is no significant change in other types of immune cells. **D.** Histologic and CD117 immunohistochemical analyses confirming the increase of mast cells in the TIME of NAT-treated PDAC. (* $p<0.05$; ** $p<0.01$; # $p<0.1$)

Figure. 5 NAT-induced upregulation of TME complement expression as a positive prognostic biomarker for NAT-treated PDAC. **A.** Heatmap displaying the expression levels of the five NAT-upregulated complement genes in the TME of the NAT group. Unsupervised clustering effectively stratified them into the high TME complement subgroup (on the left side) and low complement subgroup (on the right side). **B.** Kaplan-Meier curve showing that the high TME complement subgroup (red line) has a significantly improved overall survival compared to the low TME complement subgroup (blue line, $p=0.02$) and a marginally improved overall survival compared to the naïve group (green line, $p=0.09$) (* $p<0.05$; # $p<0.1$). There is no statistically significant difference in overall survival between the low TME complement subgroup and the naïve group. **C.** Forest plot of the stratified multivariate Cox proportional hazards model identifying the TME complement level as an independent favorable prognostic factor for NAT-treated patients (HR=0.21; 95% CI: 0.06-0.51, $p=0.023$). Positive surgical resection margin (R1) is identified as an independent poor prognostic factor for NAT-treated patients (HR=5.46; 95% CI: 1.28-23.27, $p=0.022$).

Figure. 6 Association of NAT-induced upregulation of TME complement expression with immunomodulation and decreased immune exhaustion. **A.** Box-Whisker plot showing that the high TME complement subgroup has significantly increased mast cells, CD4+ T cells and monocytes compared to the low TME complement subgroup (* $p<0.05$). **B.** The high TME complement subgroup has significantly increased immunomodulatory CAFs compared to the low TME complement group. In addition, the TME of the high TME complement group has significantly decreased immune exhaustion signature score and no significant change in immune cytotoxicity signature score (* $p<0.05$; *** $p<0.001$). **C.** Schematic representation summarizing how NAT differentially modulates carcinoma and TME of PDAC. While NAT mainly increases the apoptosis and decreases the proliferation and G2/M phase cycling in carcinoma cells, it has broad immunomodulatory effects on the TME through upregulating complement signaling.

Supplementary Figures

Supplementary Figure. 1 The overall experimental Design.

Supplementary Figure. 2 The volcano plots of DEGs in carcinoma AOIs and TME AOIs in the naïve group and the NAT group.

Supplementary Figure. 3 Immune cell distribution in carcinoma and TME AOIs across the study cohort. The TME AOIs exhibit significantly greater abundance and diversity of immune cells compared to the carcinoma AOIs.

Supplementary Figure. 4 Paired analysis of pre-NAT biopsy and post-NAT resection from the same patient. A. Among the four patients for whom both the pre-NAT biopsy and post-NAT resection were available, two of them exhibited NA- induced upregulation of C3 complement level in TME, while the other two patients showed no increase. **B.** The two patients with NAT-induced upregulation of TME C3 complement level showed better overall survival.

References:

1 Siegel, R. L., Miller, K. D., Fuchs, H. E. & Jemal, A. Cancer statistics, 2022. *CA Cancer J Clin* **72**, 7-33, doi:10.3322/caac.21708 (2022).

2 Rahib, L., Wehner, M. R., Matrisian, L. M. & Nead, K. T. Estimated Projection of US Cancer Incidence and Death to 2040. *JAMA Netw Open* **4**, e214708, doi:10.1001/jamanetworkopen.2021.4708 (2021).

3 Vincent, A., Herman, J., Schulick, R., Hruban, R. H. & Goggins, M. Pancreatic cancer. *Lancet* **378**, 607-620, doi:10.1016/S0140-6736(10)62307-0 (2011).

4 Ferrone, C. R. *et al.* Pancreatic adenocarcinoma: the actual 5-year survivors. *J Gastrointest Surg* **12**, 701-706, doi:10.1007/s11605-007-0384-8 (2008).

5 Wood, L. D., Canto, M. I., Jaffee, E. M. & Simeone, D. M. Pancreatic Cancer: Pathogenesis, Screening, Diagnosis, and Treatment. *Gastroenterology* **163**, 386-402 e381, doi:10.1053/j.gastro.2022.03.056 (2022).

6 Collisson, E. A., Bailey, P., Chang, D. K. & Biankin, A. V. Molecular subtypes of pancreatic cancer. *Nat Rev Gastroenterol Hepatol* **16**, 207-220, doi:10.1038/s41575-019-0109-y (2019).

7 Shibuya, K. C. *et al.* Pancreatic ductal adenocarcinoma contains an effector and regulatory immune cell infiltrate that is altered by multimodal neoadjuvant treatment. *PLoS One* **9**, e96565, doi:10.1371/journal.pone.0096565 (2014).

8 Herting, C. J., Karpovsky, I. & Lesinski, G. B. The tumor microenvironment in pancreatic ductal adenocarcinoma: current perspectives and future directions. *Cancer Metastasis Rev* **40**, 675-689, doi:10.1007/s10555-021-09988-w (2021).

9 Murphy, J. E. *et al.* Total Neoadjuvant Therapy With FOLFIRINOX Followed by Individualized Chemoradiotherapy for Borderline Resectable Pancreatic Adenocarcinoma: A Phase 2 Clinical Trial. *JAMA Oncol* **4**, 963-969, doi:10.1001/jamaoncol.2018.0329 (2018).

10 Versteijne, E. *et al.* Neoadjuvant Chemoradiotherapy Versus Upfront Surgery for Resectable and Borderline Resectable Pancreatic Cancer: Long-Term Results of the Dutch Randomized PREOPANC Trial. *J Clin Oncol* **40**, 1220-1230, doi:10.1200/JCO.21.02233 (2022).

11 Attaallah, W. Neoadjuvant Chemoradiotherapy for Resectable and Borderline Resectable Pancreatic Cancer. *J Clin Oncol* **40**, 3346, doi:10.1200/JCO.22.00432 (2022).

12 Manrai, M., Tilak, T., Dawra, S., Srivastava, S. & Singh, A. Current and emerging therapeutic strategies in pancreatic cancer: Challenges and opportunities. *World J Gastroenterol* **27**, 6572-6589, doi:10.3748/wjg.v27.i39.6572 (2021).

13 Krishnamoorthy, M., Lenehan, J. G. & Maleki Vareki, S. Neoadjuvant Immunotherapy for High-Risk, Resectable Malignancies: Scientific Rationale and Clinical Challenges. *J Natl Cancer Inst* **113**, 823-832, doi:10.1093/jnci/djaa216 (2021).

14 Kuipers, J., Jahn, K. & Beerenwinkel, N. Advances in understanding tumour evolution through single-cell sequencing. *Biochim Biophys Acta Rev Cancer* **1867**, 127-138, doi:10.1016/j.bbcan.2017.02.001 (2017).

15 Lahnemann, D. *et al.* Eleven grand challenges in single-cell data science. *Genome Biol* **21**, 31, doi:10.1186/s13059-020-1926-6 (2020).

16 Han, J., DePinho, R. A. & Maitra, A. Single-cell RNA sequencing in pancreatic cancer. *Nat Rev Gastroenterol Hepatol* **18**, 451-452, doi:10.1038/s41575-021-00471-z (2021).

17 Peng, J. *et al.* Single-cell RNA-seq highlights intra-tumoral heterogeneity and malignant progression in pancreatic ductal adenocarcinoma. *Cell Res* **29**, 725-738, doi:10.1038/s41422-019-0195-y (2019).

599 18 Raghavan, S. *et al.* Microenvironment drives cell state, plasticity, and drug response in
600 pancreatic cancer. *Cell* **184**, 6119-6137 e6126, doi:10.1016/j.cell.2021.11.017 (2021).
601 19 Hwang, W. L. *et al.* Single-nucleus and spatial transcriptome profiling of pancreatic cancer
602 identifies multicellular dynamics associated with neoadjuvant treatment. *Nat Genet* **54**, 1178-
603 1191, doi:10.1038/s41588-022-01134-8 (2022).
604 20 Werba, G. *et al.* Single-cell RNA sequencing reveals the effects of chemotherapy on human
605 pancreatic adenocarcinoma and its tumor microenvironment. *Nat Commun* **14**, 797,
606 doi:10.1038/s41467-023-36296-4 (2023).
607 21 Ma, Y. & Zhou, X. Spatially informed cell-type deconvolution for spatial transcriptomics. *Nat*
608 *Biotechnol* **40**, 1349-1359, doi:10.1038/s41587-022-01273-7 (2022).
609 22 Dardare, J. *et al.* DDB2 represses epithelial-to-mesenchymal transition and sensitizes pancreatic
610 ductal adenocarcinoma cells to chemotherapy. *Front Oncol* **12**, 1052163,
611 doi:10.3389/fonc.2022.1052163 (2022).
612 23 Krauss, L. *et al.* HDAC2 Facilitates Pancreatic Cancer Metastasis. *Cancer Res* **82**, 695-707,
613 doi:10.1158/0008-5472.CAN-20-3209 (2022).
614 24 Merle, N. S., Noe, R., Halbwachs-Mecarelli, L., Fremeaux-Bacchi, V. & Roumenina, L. T.
615 Complement System Part II: Role in Immunity. *Front Immunol* **6**, 257,
616 doi:10.3389/fimmu.2015.00257 (2015).
617 25 Chen, K. *et al.* Single-cell RNA-seq reveals dynamic change in tumor microenvironment during
618 pancreatic ductal adenocarcinoma malignant progression. *EBioMedicine* **66**, 103315,
619 doi:10.1016/j.ebiom.2021.103315 (2021).
620 26 Croft, W. *et al.* Spatial determination and prognostic impact of the fibroblast transcriptome in
621 pancreatic ductal adenocarcinoma. *Elife* **12**, doi:10.7554/eLife.86125 (2023).
622 27 Shiau, C. *et al.* Therapy-associated remodeling of pancreatic cancer revealed by single-cell
623 spatial transcriptomics and optimal transport analysis. *bioRxiv*, doi:10.1101/2023.06.28.546848
624 (2023).
625 28 West, E. E. & Kemper, C. Complosome - the intracellular complement system. *Nat Rev Nephrol*
626 **19**, 426-439, doi:10.1038/s41581-023-00704-1 (2023).
627 29 Huang da, W., Sherman, B. T. & Lempicki, R. A. Systematic and integrative analysis of large gene
628 lists using DAVID bioinformatics resources. *Nat Protoc* **4**, 44-57, doi:10.1038/nprot.2008.211
629 (2009).
630 30 Sherman, B. T. *et al.* DAVID: a web server for functional enrichment analysis and functional
631 annotation of gene lists (2021 update). *Nucleic Acids Res* **50**, W216-W221,
632 doi:10.1093/nar/gkac194 (2022).

Figure. 1

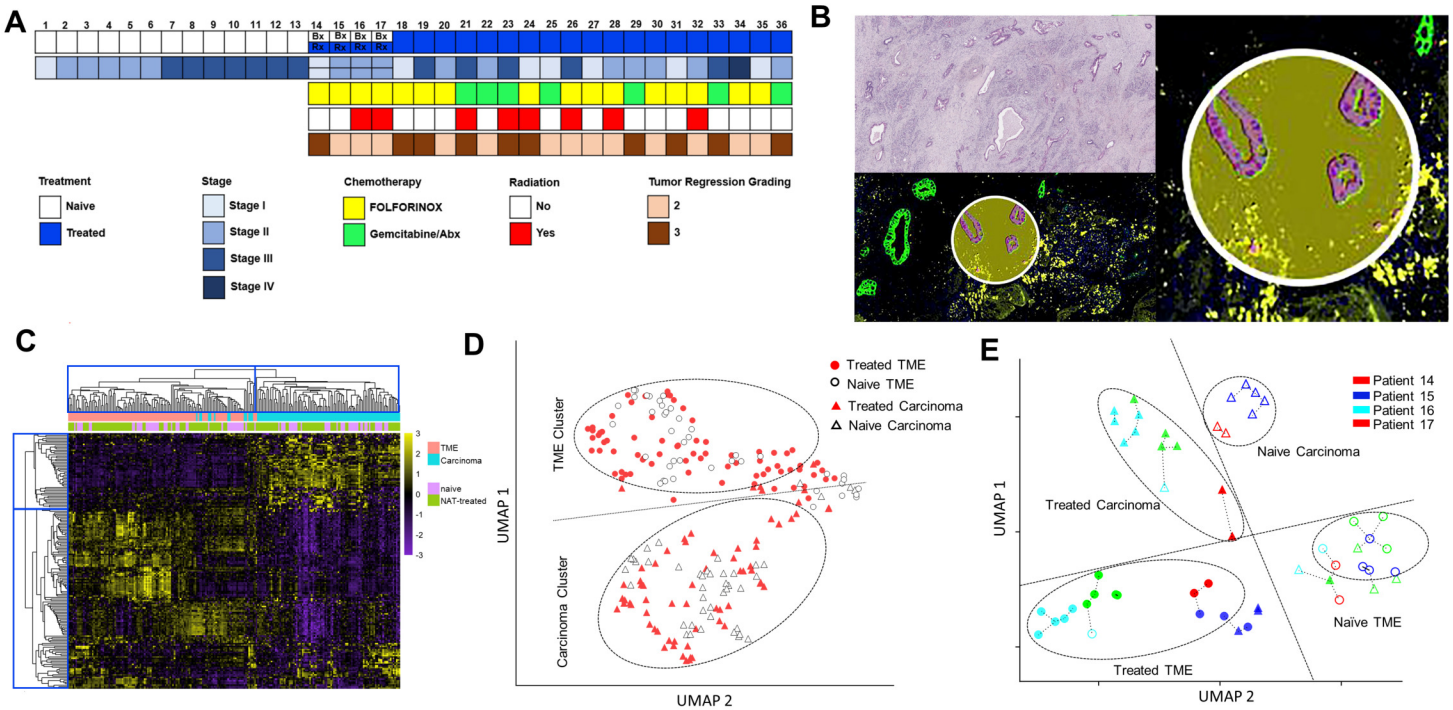
A
Treatment
Naive
Treated
Stage
Stage I
Stage II
Stage III
Stage IV
Chemotherapy
FOLFORINOX
Gemcitabine/Abx
Radiation
No
Yes
Tumor Regression Grading
2
3
B
C
TME
Carcinoma
naive
NAT-treated
D
Treated TME
Naive TME
Treated Carcinoma
Naive Carcinoma
TME Cluster
Carcinoma Cluster
UMAP 1
UMAP 2
E
Patient 14
Patient 15
Patient 16
Patient 17
Naive Carcinoma
Treated Carcinoma
Naïve TME
Treated TME
UMAP 1
UMAP 2

Figure. 2

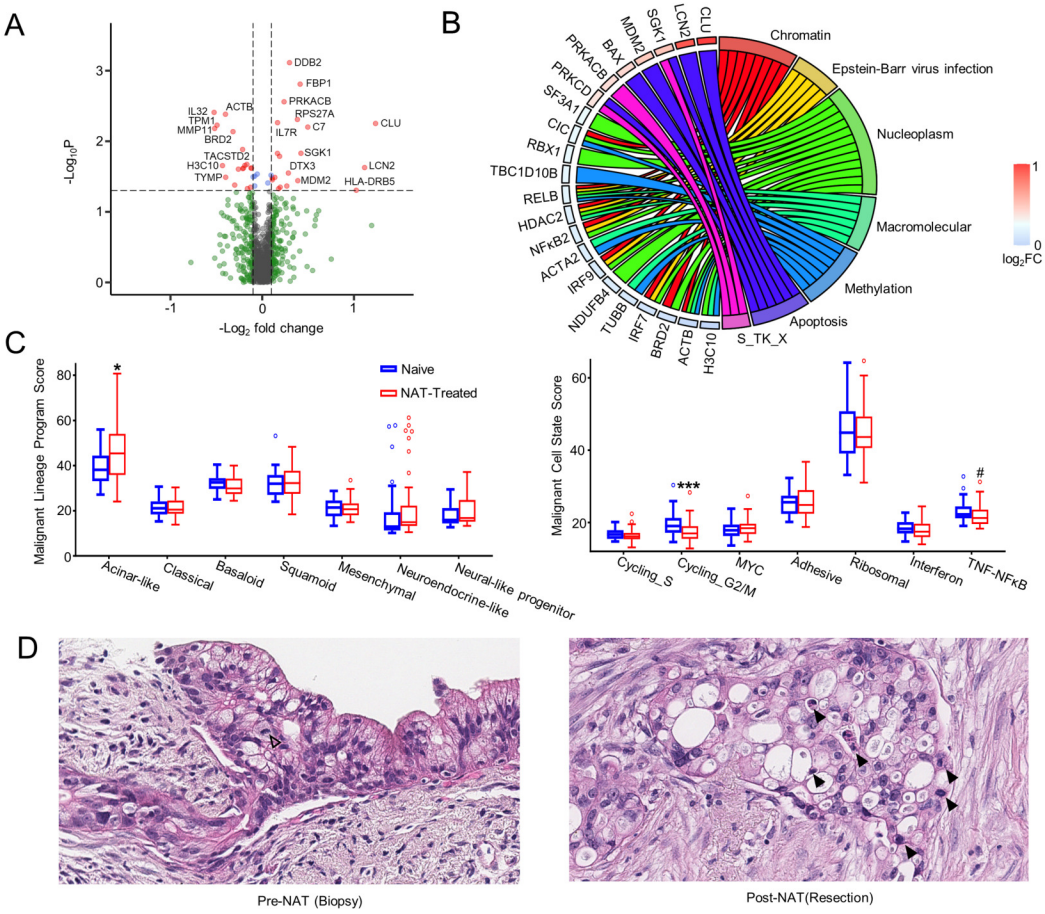
A
DDB2
FBP1
PRKACB
RPS27A
C7
CLU
IL32
ACTB
TPM1
MMP11
BRD2
IL7R
SGK1
TACSTD2
H3C10
TYMP
DTX3
LCN2
MDM2
HLA-DRB5
-Log10P
-Log2 fold change
B
Chromatin
Epstein-Barr virus infection
Nucleoplasm
Macromolecular
Methylation
Apoptosis
S_TK_X
H3C10
ACTB
BRD2
IRF7
TUBB
NDUFB4
IRF9
ACTA2
NFκB2
HDAC2
RELB
TBC1D10B
RBX1
CIC
SF3A1
PRKCD
PRKACB
BAX
MDM2
SGK1
LCN2
CLU
log2FC
C
Naive
NAT-Treated
Malignant Lineage Program Score
Acinar-like
Classical
Basaloid
Squamoid
Mesenchymal
Neuroendocrine-like
Neural-like progenitor
Malignant Cell State Score
Cycling_S
Cycling_G2/M
MYC
Adhesive
Ribosomal
Interferon
TNF-NFκB
D
Pre-NAT (Biopsy)
Post-NAT(Resection)

Figure. 3

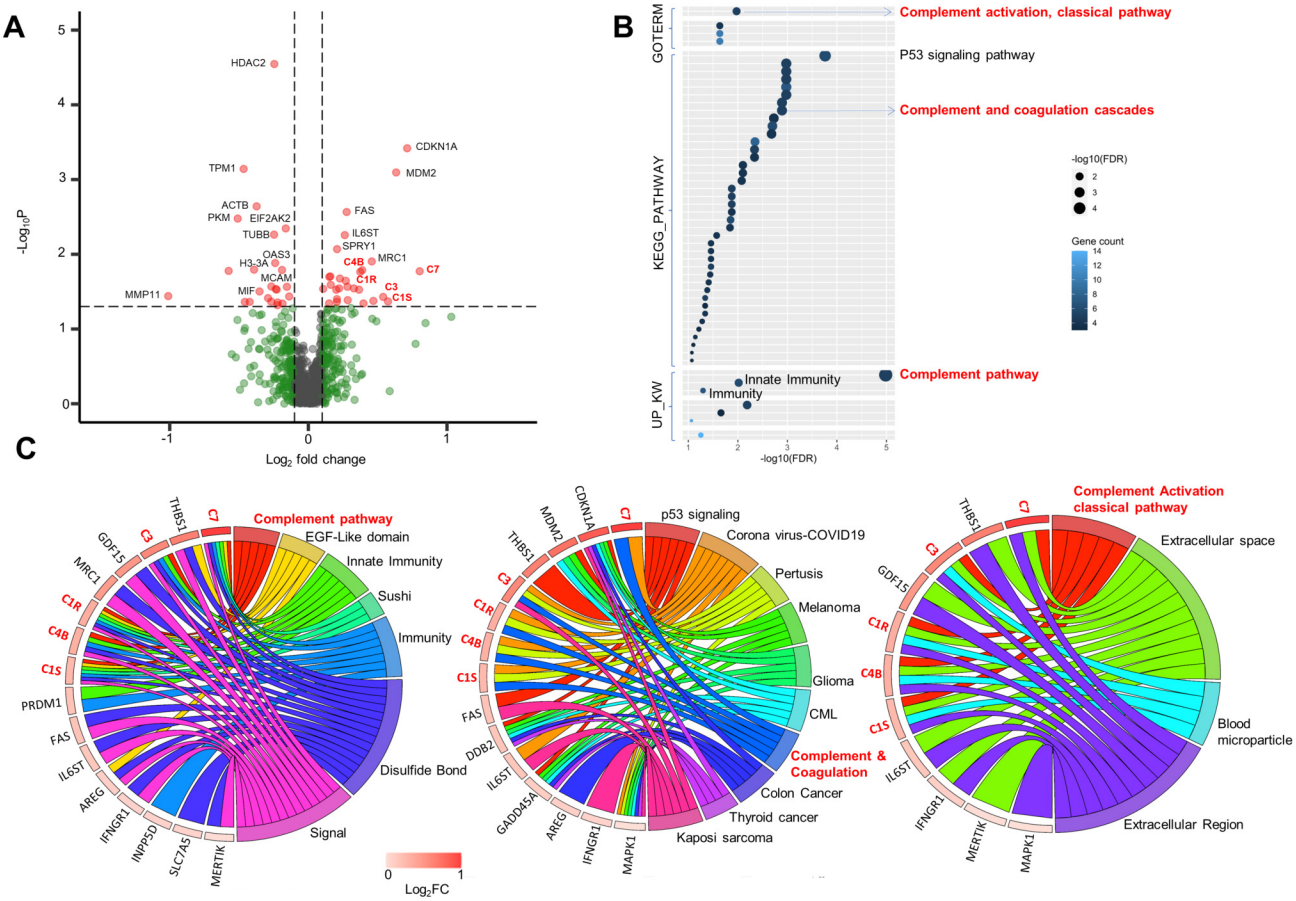
A
HDAC2
CDKN1A
MDM2
TPM1
ACTB
PKM
EIF2AK2
TUBB
FAS
IL6ST
SPRY1
OAS3
H3-3A
MCAM
MIF
MRC1
C4B
C1R
C7
C3
C1S
MMP11
-Log10P
Log2 fold change
B
GOTERM
KEGG_PATHWAY
UP_KW
Complement activation, classical pathway
P53 signaling pathway
Complement and coagulation cascades
Complement pathway
Innate Immunity
Immunity
-log10(FDR)
Gene count
C
Complement pathway
EGF-Like domain
Innate Immunity
Sushi
Immunity
Disulfide Bond
Signal
p53 signaling
Corona virus-COVID19
Pertusis
Melanoma
Glioma
CML
Complement & Coagulation
Colon Cancer
Thyroid cancer
Kaposi sarcoma
Complement Activation classical pathway
Extracellular space
Blood microparticle
Extracellular Region
Log2FC

Figure. 4

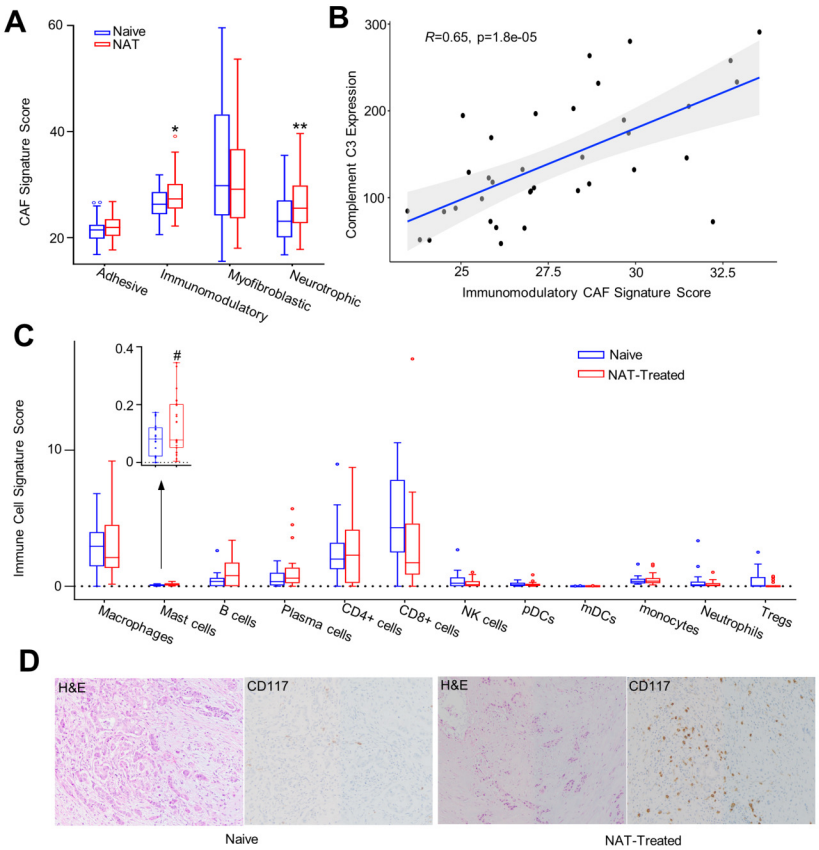
A
Naive
NAT
CAF Signature Score
60
40
20
*
**
Adhesive
Immunomodulatory
Myofibroblastic
Neurotrophic
B
R=0.65, p=1.8e-05
Complement C3 Expression
300
200
100
25
27.5
30
32.5
Immunomodulatory CAF Signature Score
C
Naive
NAT-Treated
Immune Cell Signature Score
0.4
0.2
0
#
10
0
Macrophages
Mast cells
B cells
Plasma cells
CD4+ cells
CD8+ cells
NK cells
pDCs
mDCs
monocytes
Neutrophils
Tregs
D
H&E
CD117
H&E
CD117
Naive
NAT-Treated

Figure. 5

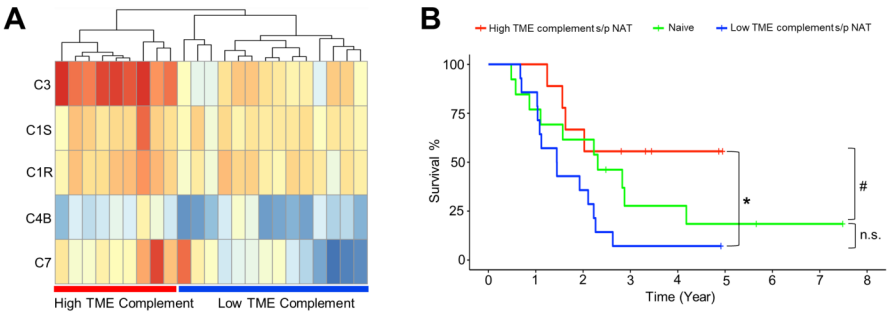

C

Covariate (# of subjects)	Stratified Multivariate Hazard Ratio (95% CI), adjusted p value
Complement – Low (14/23)	Reference
Complement – High (9/23)	0.21 (0.06, 0.81) 0.023
Margin – R0 (15/23)	Reference
Margin – R1 (8/23)	5.46 (1.28, 23.27) 0.022
Gender – Female (14/23)	Reference
Gender – Male (9/23)	1.36 (0.29, 6.36) 0.692
T-stage – Confine to Pancreas (20/23)	Reference
T-stage – Grow out of Pancreas (3/23)	2.41 (0.41, 14.28) 0.334
Grading – G1 (3/23)	Reference
Grading – G2 (12/23)	1.54 (0.20, 12.11) 0.682
Grading – G3 (8/23)	4.83 (0.79, 29.66) 0.089
Lymph node metastasis – N0 (11/23)	Reference
Lymph node metastasis – N1 (12/23)	2.56 (0.62, 10.56) 0.192

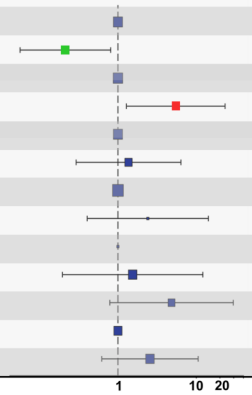

Figure. 6

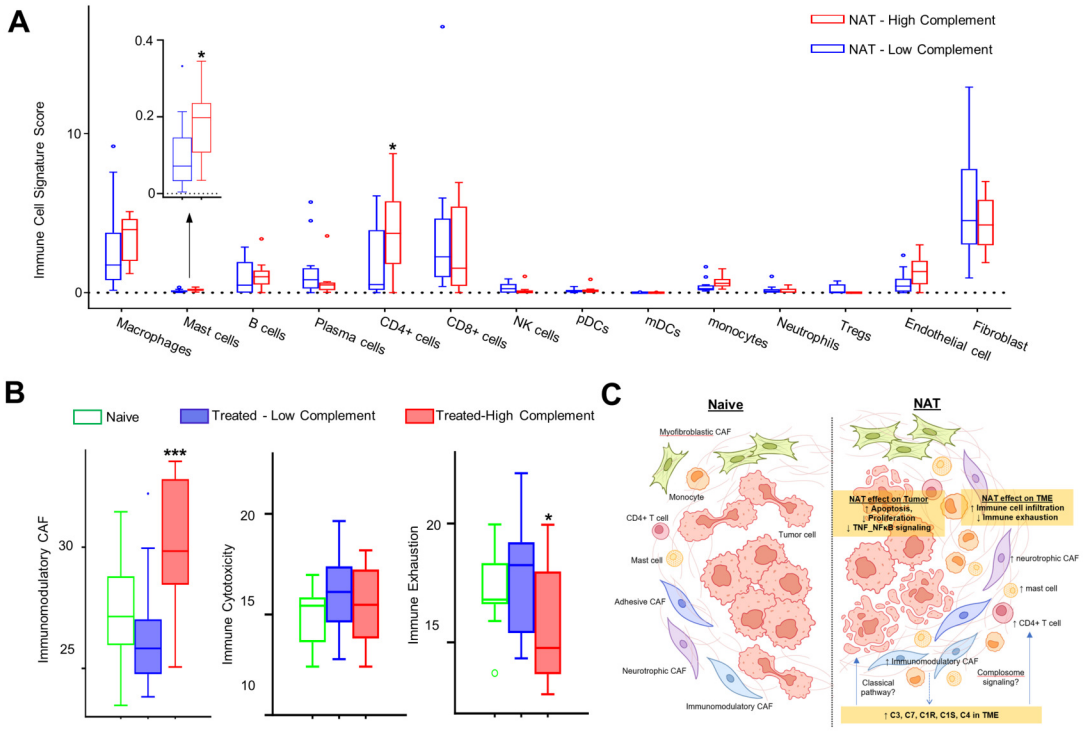
A
NAT - High Complement
NAT - Low Complement
Immune Cell Signature Score
Macrophages
Mast cells
B cells
Plasma cells
CD4+ cells
CD8+ cells
NK cells
pDCs
mDCs
monocytes
Neutrophils
Tregs
Endothelial cell
Fibroblast
B
Naive
Treated - Low Complement
Treated-High Complement
Immunomodulatory CAF
Immune Cytotoxicity
Immune Exhaustion
C
Naive
NAT
Myofibroblastic CAF
Monocyte
CD4+ T cell
Tumor cell
Mast cell
Adhesive CAF
Neurotrophic CAF
Immunomodulatory CAF
NAT effect on Tumor
↑ Apoptosis,
↓ Proliferation
↓ TNF_NFκB signaling
NAT effect on TME
↑ Immune cell infiltration
↓ Immune exhaustion
↑ neurotrophic CAF
↑ mast cell
↑ CD4+ T cell
↑ Immunomodulatory CAF
Classical pathway?
Complosome signaling?
↑ C3, C7, C1R, C1S, C4 in TME